Trap Characterization of Trench-Gate SiC MOSFETs Based on Transient Drain Current

Shan Jiang, Meng Zhang, Xianwei Meng, Xiang Zheng, Shiwei Feng, and Yamin Zhang

***Abstract*—The SiC/SiO_2 interface state is one of the main factors that limit the performance and reliability of the SiC metal–oxide–semiconductor field-effect transistor (MOSFET). In this article, we use a Bayesian deconvolution algorithm to optimize trap feature extraction based on the transient current method and improve the trap extraction accuracy. Using this method, we study the trap capture mechanism in SiC MOSFETs and mainly characterize the trap position, the trap energy level, and the capture time constant. The results obtained show that there are three different types of traps and defects, two of which are SiC interface traps at the gate–source and gate–drain interfaces, with activation energies of 0.089 and 0.035 eV, respectively, and the third trap type is an oxide trap, and its time constant does not vary with temperature. The characterization results are verified via deep-level transient spectroscopy, and the results show reasonable agreement with those obtained by the method proposed in this article. This method can be combined with electrical stress testing in long-term reliability research to realize nondestructive characterization of the defects of SiC MOSFETs.**

***Index Terms*—Charge trapping, current transient, reliability, SiC metal–oxide–semiconductor field-effect transistor (MOSFET), trench silicon carbide MOSFET.**

I. Introduction

SIC-BASED power electronic devices have the advantages of a wide band gap, high thermal conductivity, and high breakdown field strength. These devices are suitable for use under high temperature, high frequency, and high power conditions, and are highly advantageous in reducing both power consumption and system volume; the latter two issues are focusing the attention of researchers worldwide. However, in high-frequency and high-power applications, reliability issues including high temperatures in the active region, device threshold voltage drift, on-resistance degradation, and gate oxide defects are the main issues that have stopped SiC-based power devices from becoming mature industrialized products [1], [2], [3], [4].

In SiC metal–oxide–semiconductor field-effect transistors (MOSFETs), the gate structure is an important factor in determining the device reliability. In contrast to the higher potential barrier and lower interface state at the Si/SiO_2 interface [5], [6], the potential barrier at the SiC/SiO_2 interface is lower and the interface state is higher. Under high temperature and high field conditions, the electrons in SiC will pass through the barrier more easily and thus enter the gate dielectric. The electrons that are injected into the gate dielectric layer will not only induce defects in the dielectric but also will cause changes in the fixed charges that exist within the dielectric [7], [8], [9]. This affects the threshold voltage of the SiC MOSFET, which is the main cause of the instability in its electrical parameters [10], [11], [12].

Effective characterization of the SiC/SiO_2 interface state activation energy and concentration is an important aspect of SiC MOSFET reliability design. Moghadam et al. [13] studied and calculated the near-interface oxide trap concentration in SiC, but their trap characterization was at the material level, and they could not obtain the time constant and activation energy of the trap. Although the widely used deep-level transient spectroscopy method can measure the trap's peak value and activation energy, the test conditions required are very harsh. The device must be placed in a low-temperature environment and subjected to temperature changes over a wide range, which makes measurement of the device characteristics very difficult [14], [15], [16], [17].

Research shows that when a deep-level trap captures electrons, the drain current will decrease, and when these electrons are released, the drain current will then increase. This change in the transient current includes trap information. Therefore, the approach of measuring traps via the transient current is better than the spectroscopy method. To date, this method has been verified on GaN high-electron-mobility transistors [18], [19], [20], [21]. However, it has several problems, including low time constant accuracy, and an inability to characterize trap concentrations and traps in difficult locations that have not been verified on the SiC devices.

With the aim of solving the existing problems in interface state characterization of SiC MOSFETs, we recorded the transient curves of the drain current under a constant electrical bias at various temperatures, optimized extraction of the device time constant via the Bayesian deconvolution method, and combining with Arrhenius equation, the trap activation energy of the interface state is obtained. By varying the electrical bias of the gate

Manuscript received 20 October 2022; revised 31 December 2022; accepted 30 January 2023. Date of publication 7 February 2023; date of current version 10 March 2023. This work was supported in part by the National Key Research and Development Program of China under Grant 2022YFB3604300, in part by the National Natural Science Foundation of China under Grants 62074009 and 61804006, and in part by the Beijing Natural Science Foundation under Grants 4192012 and 4222083. Recommended for publication by Associate Editor A. Lindemann. *(Corresponding author: Yamin Zhang.)*

Shan Jiang, Meng Zhang, Xianwei Meng, Shiwei Feng, and Yamin Zhang are with the Institute of Semiconductor Device Reliability Physics, Beijing University of Technology, Beijing 100124, China (e-mail: jiangshan@emails.bjut.edu.cn; mengzhang@bjut.edu.cn; mengxw@emails.bjut.edu.cn; shwfeng@bjut.edu.cn; yaminzhang@bjut.edu.cn).

Xiang Zheng is with the Center for Device Thermography and Reliability, University of Bristol, Bristol BS8 1TL, U.K. (e-mail: xiang.zheng@bristol.ac.uk).

Color versions of one or more figures in this article are available at https://doi.org/10.1109/TPEL.2023.3242950.

Digital Object Identifier 10.1109/TPEL.2023.3242950

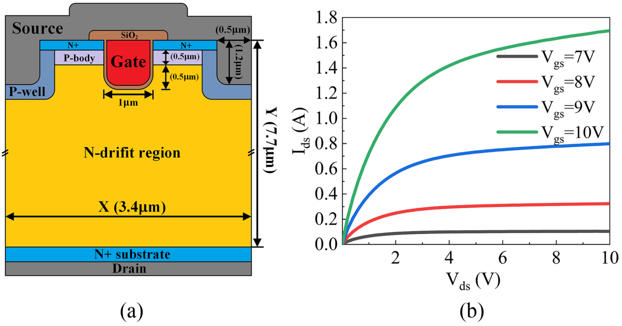

Fig. 1. (a) SiC MOSFET device cross section. (b) Output characteristic curve.

and drain, the trap positions were located, which then enabled the characterization of the interface state traps. In addition, these characterization results were verified via deep-level transient spectroscopy.

II. Trap Characterization

A. Experimental Samples and Information

A schematic diagram of the device used in this study is shown in Fig. 1(a). The device uses an epitaxial layer with a thickness of 7.7 μm to maintain a breakdown voltage of more than 650 V. A 0.5-μm-thick P-body and a 0.2-μm-thick n+ source layer were grown epitaxially on the drift region surface. The gate trench depth and width are 1.2 and 1 μm, respectively. The side gate oxide and bottom gate oxide layer thicknesses are 50 and 100 nm, respectively. Another trench that was formed in the same etching step as the gate trench is located in the source region. This source trench is wrapped by an injected p-well to protect the bottom oxide, particularly at the angle of the gate trench. The overall length of this symmetrical element is 3.4 μm. The doping concentrations of the P-body, P-well, and drift regions are 1×10^{17}, 3.5×10^{17}, and 8×10^{15} cm^{-3}, respectively. The output characteristics of the device are shown in Fig. 1(b).

B. Time Constants Extraction Method

Traps in the device cause a reduction in the drain current when electrons are trapped and an increase in the drain current when the electrons are released. Based on this relationship, the transient change in the device drain current is collected, the time constant of this drain current change caused by the trap is extracted, the change in the trap time constant under different ambient temperatures is analyzed, and by combining the results with the Arrhenius equation, the activation energy of the deep-level trap can be extracted. The accuracy of the time constant extraction process determines the accuracy of the characterization results directly.

Trap information exists in the device's transient current response in the form of an e-exponential change, as shown in the following equation:

$$I_{ds}\left(t\right) = \sum \Delta I_i \exp\left(-\frac{t}{\tau_i}\right) + I_\infty. \tag{1}$$

Here, τ_i is the time constant of the ith trap, and ΔI_i is the amplitude that affects the current change. The time constant spectrum (TCS) is mainly used to extract the trap's characteristic time constant τ_i and display it in the form of a peak spectrum, and the abscissa of this peak value is the trap's time constant.

First, we introduce the logarithmic time variable

$$z = \ln t. \tag{2}$$

The TCS of the trap is then given as follows:

$$\Delta I\left(z\right) = \lim_{\delta z\to 0} \frac{\text{magnitudes related to the time constants between } z \text{ and } z+\delta}{\delta z}. \tag{3}$$

The transient current $I_{ds}(t)$ can then be expressed in the following equation, and the TCS in (3) exists in integral form in the following equation:

$$I_{ds}\left(t\right) = \int_{-\infty}^{\infty} \Delta I\left(\tau\right)\left(\exp\left(-\frac{t}{\exp\left(\tau\right)}\right)\right) d\tau\ + I_\infty. \tag{4}$$

When compared with (1), (4) gives the integral form of the channel transient current. When combined with (2), this transient current is converted into

$$I_{ds}\left(z\right) = \int_{-\infty}^{\infty} \Delta I\left(\tau\right)\left(\exp\left(-\exp\left(z-\tau\right)\right)\right) d\tau\ + I_\infty. \tag{5}$$

This is the convolutional integral equation of $\Delta I(\tau)$. Differentiating z on both sides of (5) then gives

$$\frac{d}{dz} I_{ds}\left(z\right) = \int_{-\infty}^{\infty} \Delta I\left(\tau\right)\left(\exp\left(z-\tau-\exp\left(z-\tau\right)\right)\right) d\tau. \tag{6}$$

Function $W(z)$ is defined as follows:

$$W\left(z\right) = \exp\left(z - \exp\left(z\right)\right). \tag{7}$$

Then, the expression for $\frac{d}{dz}I_{DS}(z)$ is given by

$$\frac{d}{dz} I_{ds}\left(z\right) = -\Delta I\left(z\right) \otimes W\left(z\right). \tag{8}$$

Here, $\otimes$ is the convolution operator, and the TCS $\Delta I(z)$ then becomes

$$\Delta I\left(z\right) = \left(-\frac{d}{dz} I_{ds}\left(z\right)\right) \otimes^{-1} W\left(z\right). \tag{9}$$

Thus far, the TCS can be solved completely via deconvolution.

The key to characterization of the interface state characteristics in the transient drain current changes lies in the accuracy of the time constant extraction process. To date, three main extraction techniques have been reported. Among them, one study [18] used the sum of the e-exponents of 100 time constants (exhaustive method) to fit the transient current curve. However, this method can easily introduce "pseudovalues" into the gentle curve range and requires more predetermined conditions. Another study [22] performed a derivation of the transient curve to extract the corresponding TCS. This method is easy to solve, but cannot give the TCS in the form of an e-exponential, and its ability to distinguish overlapping peaks is inadequate. An additional study [19] used three discrete points to fit the transient

current response curve and added a variable β power correction result to the index, but it is not easy to characterize the trap time constant distribution fully using this method; moreover, the key variable β that was introduced has no clear physical meaning and cannot be used to give a one-to-one corresponding microscopic explanation.

With the aim of resolving the problem of the insufficient methods for extraction of the time constant spectra of traps, our research group studied and proposed a TCS extraction technique based on Bayesian deconvolution. By performing multiple iterative calculations, the proposed technique can not only avoid the insertion of "pseudovalues" in the nonpeak areas but also highlight the time constant peaks of traps effectively, and its discrimination ability is obviously better than that of the derivation-based method.

According to convolution theory, deconvolution problems can be solved conveniently using the fast Fourier transform method. However, the deconvolution calculation is a mathematically ill-posed problem, where the current transient response curve that acts as the input condition is the measurement result, and the noise and measurement errors introduced during the measurement process will introduce a large error into the deconvolution result. To solve this problem, we selected a Bayesian iterative algorithm [23], [24], [25], [26] according to conditional probability theory, which is based on Bayes' theorem

$$P(H|D) = \frac{P(D|H)\,P(H)}{P(D)} \tag{10}$$

where $P(H|D)$ is the conditional probability of H after the occurrence of a known D, $P(D|H)$ is the conditional probability of D after the occurrence of a known H, and $P(H)$ and $P(D)$ are the prior probabilities of H and D, respectively. Let the differential vector of the discrete transient current curve measurement result be M, let the real value vector of the time constant spectral function to be solved be T, and the transfer matrix be R. The convolution operation can then be expressed in matrix form

$$M = R \otimes T. \tag{11}$$

To solve for the true value T from (11), we can use Bayes' theorem to rewrite (11) into the form shown in the following equation:

$$P(T_i|M_k) = \frac{P(M_k|T_i)\,P(T_i)}{\sum_j P(M_k|T_j)\,P(T_j)}. \tag{12}$$

Then, based on the conditional probability formula, we can obtain

$$P(T_i) = \sum_k P(T_i|M_k)\,P(M_k). \tag{13}$$

By substituting (12) into (13), we can then obtain

$$P(T_i) = \sum_k \frac{P(M_k|T_i)\,P(T_i)\,P(M_k)}{\sum_j P(M_k|T_j)\,P(T_j)}. \tag{14}$$

Note that the $P(T_i)$ terms to be solved appear on both the left and right sides of (14), and thus form an iterative equation. The initial iteration sequence can be constructed under an assumption of equal probability, and the iteration equation after n iterations is calculated as

$$P^{(n+1)}(T_i) = P^{(n)}(T_i) \sum_k \frac{P(M_k|T_i)\,P(M_k)}{\sum_j P(M_k|T_j)\,P^{(n)}(T_j)}. \tag{15}$$

Therefore, by normalizing the test vector M of (11), the expression for the Bayesian iterative algorithm can be abbreviated as follows:

$$T_i^{n+1} = T_i^n \sum_k \frac{R_{ki} M_k}{\sum_j R_{kj} T_j^n}. \tag{16}$$

Because the Bayesian iterative method is based on probability theory, it always guarantees that the sum of the probabilities in the iterative process is 1, thus ensuring convergence of the iterative process.

To verify the effectiveness of time constant extraction based on the Bayesian iterative deconvolution operation, we constructed a function curve containing three time constants (0.2, 2, and 10 s) that are very similar. We then used the derivation method and the Bayesian iterative deconvolution operation method to extract the time constants. The results are shown in Fig. 2. The TCS calculated by Bayesian deconvolution is related to the number of iterations, and with the increasing numbers of iterations, the signal enhancement effect on the time-constant spectral line gradually becomes obvious, and the result is shown in Fig. 3.

According to (9), the TCS is the deconvolution of the current versus time ln(t) and the construction function $W(z)$. In order to obtain the TCS, first the variation of the transient current is measured. In Fig. 3(a), the original exponential decay curves with time constants of 0.2, 2, and 10 s are shown, from which the differential of current to ln(t) can be obtained. Since $W(z)$ is a self-construction function, the value of $W(z)$ can be calculated at any time t according to (7). As long as the above two known variables are deconvoluted, the final result is the TCS $\Delta\mathrm{I}(z)$. In this article, the Bayesian deconvolution method is used to deconvolute. The specific conversion process of Bayesian deconvolution is shown in (12)–(15). Expression (16) of Bayesian deconvolution can be obtained by bringing $P(T_i) = \frac{T_i}{\sum_j T_j}$ $P(M_k) = \frac{M_k}{\sum_j M_j}$ $P(M_k|T_i) = \frac{R_{ki}}{\sum_j R_{kij}}$ into (15), where T_i is the TCS to be calculated, M_k represents the differential quantity of current versus time, R_{ki} denotes the construction function $W(z)$. Fig. 2(c) shows the result of Bayesian deconvolution through (16).

The TCS that was extracted from the original curve using the derivative method is shown in Fig. 3(b). By comparing the derivation method with the method based on Bayesian iteration, we see that for the trap peaks obtained using the derivation method, the time constants of 0.2 and 2 s are too close to each other to distinguish. In addition, the strong peak signal with a time constant of 10 s can hardly be recognized. In the TCS extracted using the Bayesian iterative method, the trap peak is shown clearly, and the time constant is extracted accurately. The comparison shows that the time constant extraction method based on Bayesian iteration offers obvious advantages in terms

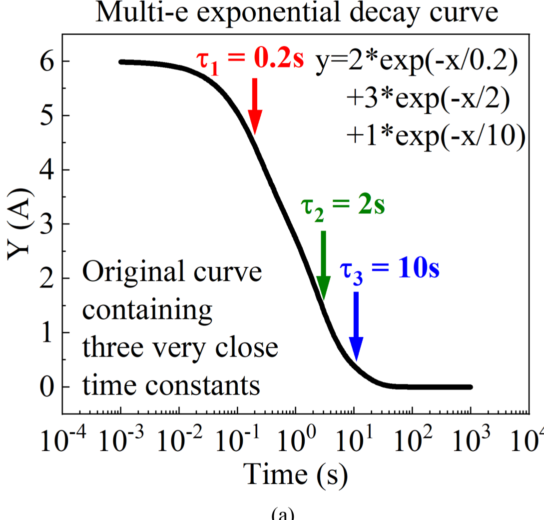

(a)

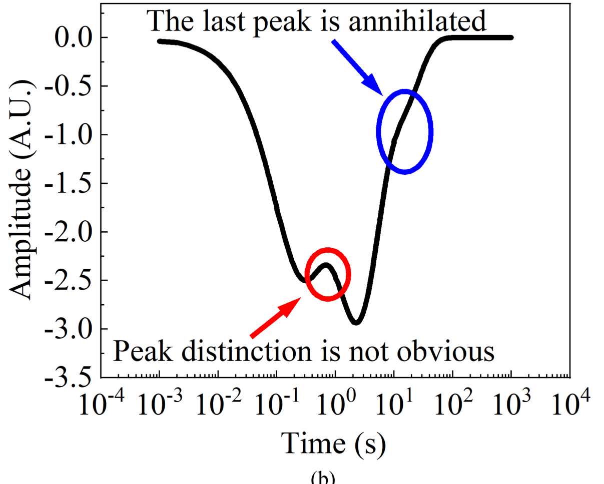

(b)

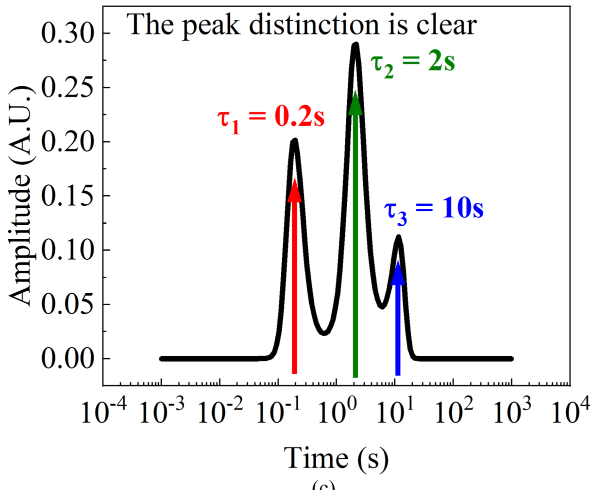

(c)

Fig. 2. (a) Construction curve containing time constant of 0.2, 2, and 10 s. (b) TCS calculated by the derivative method. (c) TCS calculated by Bayesian deconvolution.

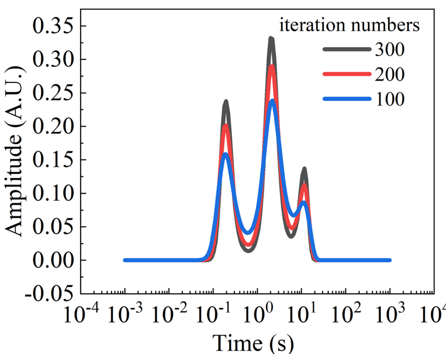

Fig. 3. Influence of different iteration numbers on TCS calculated by Bayesian deconvolution.

TABLE I
TIME CONSTANT ERROR

Time constant of construction (s)	Calculated time constant (s)	relative error (%)
0.2	0.196	1.68
2	2.087	4.35
10	10.366	3.66

of trap time constant extraction accuracy and the distinction of nearest neighbor time constants.

Fig. 3 plots the TCS calculated under different iterations using the data in Fig. 2(a). It can be seen that the peak value of the trap increases with iteration numbers, which confirms that the number of Bayesian deconvolution iterations enhances the signal effect. Table I presents the calculated error between the construction time constant and the actually calculated time constant. The minimum error is about 1%, the maximum error is about 5%, and the average error is about 2%.

C. Trap Activation Energy Characterization Using Bayesian Deconvolution Transient Current Method

To obtain both the location and the activation energy of the trap, we record the transient changes in the device drain current, apply the Bayesian iterative deconvolution algorithm to extraction of the time constant, analyze the changes in the trap time constant under various ambient temperatures, and then extract the deep-level trap's activation energy in combination with the Arrhenius equation. This procedure includes the following main steps.

1) Collect the transient changes in the drain current occurring under different ambient temperature conditions.
2) Extract the time constant of the drain current transient response curve.
3) Using the Arrhenius equation, calculate the trap activation energy based on the change in the time constant with temperature.

To obtain the transient change curve for the drain current, which contains the trap information, we first apply an electrical bias between the gate and source electrodes (gate–source voltage

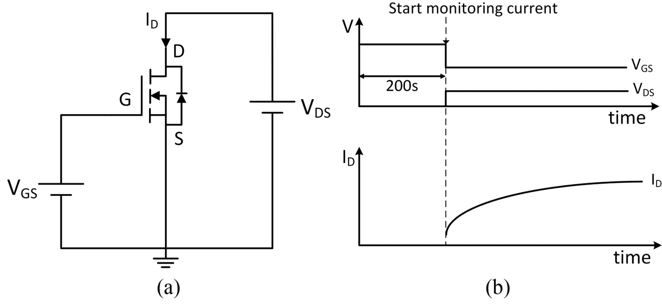

Fig. 4. (a) Testing circuit schematic diagram. (b) Bias sequence.

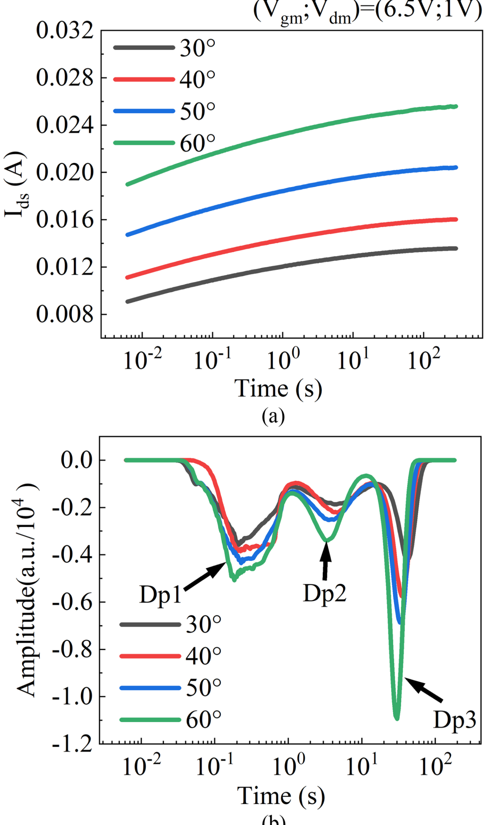

Fig. 5. (a) Transient current curve. (b) Time constant plot.

$V_{gs} = 8$ V; drain-source voltage $V_{ds} = 0$ V) for 200 s to ensure that the trap is fully filled with electrons. The electrical bias is then converted from the filling state into the measurement state, and the transient change in the drain current is collected simultaneously. The sampling time interval is 1 ms, and the sampling instrument is the Agilent B1505 analyzer. Because the drain current change is mainly affected by the trap and self-heating, we set the drain electrical bias in the acquisition state to (gate–source voltage for measurement $V_{gm} = 6.5$ V; drain-source voltage for measurement $V_{dm} = 1$ V) to avoid the influence of self-heating. Under these electrical bias conditions, the drain current is less than 50 mA, the dissipated power is approximately 0.05 W, the device thermal resistance is 1.12 °C/W when the heat dissipation is good, and the temperature change in the active region caused by these test conditions is approximately 0.056 °C. It can thus be considered approximately that the influence of self-heating can be ignored. The specific electrical connections and bias sequence used in the measurement process are shown in Fig. 4.

The platform temperature was changed, causing the temperature to rise from 30 °C to 60 °C in steps of 10 °C. The steps above were then repeated at the various temperature points above, but with an interval of 6 h between the two measurement processes, and each electrode was short circuited after addition of the reverse bias to the gate–source electrode for a period of time to accelerate the recovery of the device [27], avoid any impact of repeated measurements on the trap state, and ensure the repeatability of the measurement results. The transient change curve for the drain current caused by the trap state at the different temperatures is shown in Fig. 5(a).

When the Bayesian iterative deconvolution time constant extraction method described in Section II-B is used to extract the time constants of the transient current response curves at the different temperatures, as illustrated in Fig. 5(b), the figure shows that three time constant peaks can be extracted from each curve, and the amplitudes of these peaks increase with increasing temperature, indicating that larger numbers of carriers are injected into the interface state when the temperature increases. Among these characteristics, the time constant of Dp1 remains almost unchanged, whereas the time constants of Dp2 and Dp3 decrease gradually with increasing temperature (Dp refers to the trap calculated by the transient current method of Bayesian deconvolution).

Using the change in the time constant in combination with the Arrhenius equation [28], we obtain

$$e_n = \gamma_n \sigma_n T^2 \exp\left(-\frac{E_a}{kT}\right) \tag{17}$$

where e_n is the electron emissivity, σ_n is the trap density, γ_n is the exponential factor, T is the temperature of the device's active region, and τ is the time constant of the trap at this temperature, which is related to the electron emissivity e_n in a reciprocal relationship, i.e., $e_n = \tau^{-1}$. Additionally, k is the Boltzmann constant, and E_a is the activation energy.

The required formula can then be obtained by performing an equivalent transformation and taking the following numbers:

$$\ln\left(\frac{1}{T^2\tau_n}\right) = \ln\left(\gamma_n \sigma_n \exp\left(-\frac{E_a}{kT}\right)\right) \tag{18}$$

$$\ln\left(T^2\tau_n\right) = E_a \frac{1}{kT} - \ln\left(\gamma_n \sigma_n\right). \tag{19}$$

Here, $\ln(T^2\tau_n)$ is the ordinate and $1/kT$ is the abscissa. The linear slope produced by plotting the values obtained at the different temperatures gives the activation energy for the corresponding trap.

Finally, the activation energies of Dp2 and Dp3 are calculated to be 0.035 and 0.089 eV, respectively, using the Arrhenius equation formula. The results are shown in Fig. 6. Because there is no movement in Dp1, its activation energy cannot be calculated. If the maximum error of about 5% in Table I is

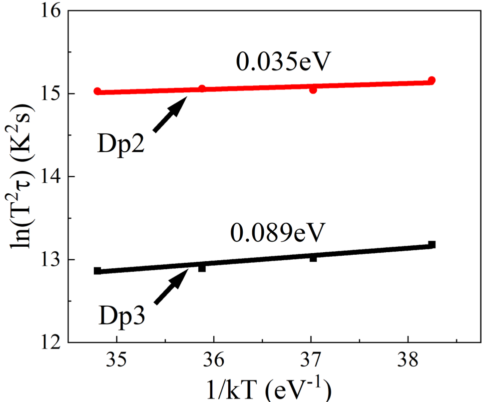

Fig. 6. Activation energy of Dp2 and Dp3.

considered, the substitution calculation has little influence on the extraction of the final activation energy, and it can be almost ignored.

Since Dp1 hardly changes with temperature, the trap may be caused by Fowler Nordheim tunneling effect. When the barrier height reaches a certain value due to the applied voltage, electrons will tunnel directly into the oxide layer regardless of the barrier height. Many previous studies [29], [30], [31] reported the influence of Fowler Nordheim tunneling on device characteristics. According to [31], the temperature coefficient of Fowler Nordheim electron barrier height is a very small negative number ($d\varphi B/dT = -0.98\,\mathrm{meV}/^\circ\mathrm{C}$), which also confirms the possibility that Dp1 is Fowler Nordheim tunneling. As the barrier height temperature coefficient is negative, when the temperature rises, the Fowler Nordheim electron barrier height decreases slightly under the same electric field strength. The probability of electron tunneling increases slightly, which is reflected in Fig. 5(b), and the amplitude of Dp1 only increases slightly. The amplitude changes of Dp2 and Dp3 are obviously larger than Dp1, because Dp2 and Dp3 are traps caused by hot carrier injection. With the increase in temperature, more and more hot carriers are excited and injected, resulting in significant changes in amplitude.

D. Trap Activation Energy Characterization Using Deep-Level Transient Spectroscopy

To verify the accuracy of the experimentally obtained activation energy characterization results obtained above, we tested the traps of the device via deep-level transient spectroscopy.

The deep-level transient spectrum (DLTS) is used to calculate the trap information based on the transient change of metal–oxide–semiconductor (MOS) capacitance. At time t, the MOS capacitance difference between t and the steady state is

$$\Delta C\left(t\right) = \Delta C_0 e^{-\frac{t}{\tau}}. \tag{20}$$

It can also be seen from (17) that e_n is a function of temperature. The DLTS technology takes advantage of the temperature characteristics of e_n and sets an "emissivity window" to obtain $e_n(T)$ from the capacitance transient, thus obtaining the basic physical parameters of the deep level.

The "emissivity window" means that the capacitor is transiently sampled and subtracted by the sampling average at fixed times t_1 and t_2 after the pulse, that is, the output of the sampling average is

$$\begin{aligned} S\left(T\right) &= \Delta C\left(t_2\right) - \Delta C\left(t_1\right) \\ &= \Delta C_0 \left(e^{-t_1 e_n(T)} - e^{-t_2 e_n(T)}\right). \end{aligned} \tag{21}$$

If the temperature changes, both $e_n(T)$ and $S(T)$ will be different. The extreme value of the above formula can be found, when $T = T_m$, where T_m meets

$$e_n\left(T_m\right) = \frac{\ln\left(\frac{t_2}{t_1}\right)}{t_2 - t_1}. \tag{22}$$

At the same energy level, the selected values of t_{1i} and t_{2i} are different, and the values of emissivity $e_n(T_{mi})$ at the different extremum temperatures T_{mi} can then be obtained. By bringing $e_n = \tau^{-1}$ into (19), we know that $ln\frac{e_n}{T^2}$ is a straight line with respect to $\frac{1}{T}$, its slope is $-\frac{E_a}{T}$, and its intercept is related to σ_n. According to the obtained values of emissivity $e_n(T_{mi})$ at the different temperatures T_{mi}, E_a can be obtained from $\ln\frac{e_n}{T^2} - \frac{1}{T}$ to give the activation energy information.

The capacitance deep-level transient spectroscopy (C-DLTS) test was conducted on the SiC MOSFET with a reverse voltage $V_R = -1$ V and a forward fill pulse bias $V_p = 5$ V, and the pulsewidth (t_p) was 250 μs. By selecting a sufficiently large t_1 value and only counting the signals that were generated after hole recovery, interference from the hole recovery process in the well state analysis can be avoided. The C-DLTS spectrum in the rate window between $t_1 = 1.96$ ms and $t_2 = 48.13$ ms is shown in Fig. 7(a) within the temperature range from 50 to 500 K.

The peak position in Fig. 7 has changed and can be determined according to T_W and e_n given. It can be seen from (20) that the temperature T is determined by $\frac{\ln(\frac{t_2}{t_1})}{t_2 - t_1}$ when the peak occurs. Since $T_W = t_2 - t_1$, it can be seen from the derivation in (22) that $e_n(T_m)$ is a subtractive function within the normal value range of T_W ($T_W > 0$), that is, $e_n(T_m)$ will decrease with the increase of T_W. According to (17) that when $E_a > 0$, e_n increases with T. In summary, when T_W increases, T_m will decrease, resulting in the peak moving to the left.

Two peaks, denoted by Trp1 and Trp2 (Trp is the activation energy calculated using DLTS), were obtained through DLTS testing. However, because the Trp2 peak does not obviously change, the activation energy of this trap cannot be calculated. Finally, only the activation energy of Trp1 can be calculated, and it is 0.088 eV. The results are shown in Fig. 7(b). Comparison of these results with those measured by the method proposed in this article shows that the activation energy of Trp1 is almost the same as that of Dp3 when calculated using the proposed method, whereas the characteristic for Trp2 is consistent with that of Dp1. The activation energies cannot be calculated for the latter peaks and they show almost no change with temperature; Dp2 has no corresponding peak in DLTS, and the specific reason for this will be discussed when studying trap locations in Section III-B.

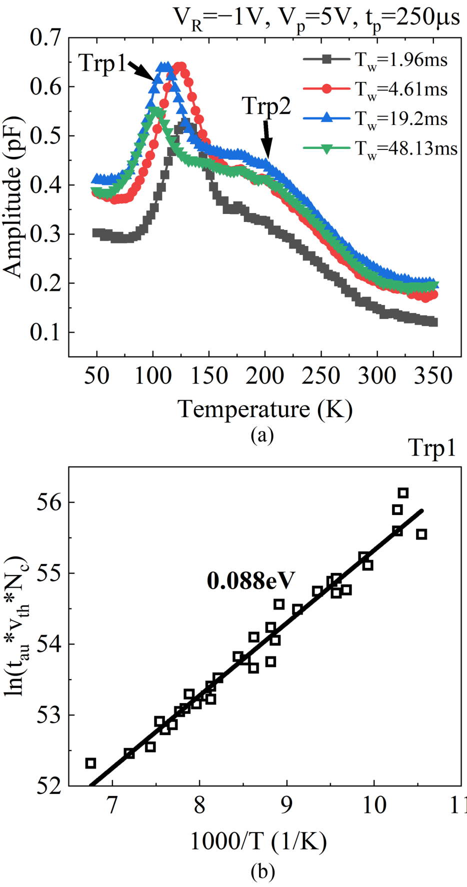

Fig. 7. (a) Spectral diagram of C-DLTS when the reverse voltage $V_R = -1$ V and the pulse voltage $V_P = 5$ V. (b) Trap activation energy characteristics measured by DLTS.

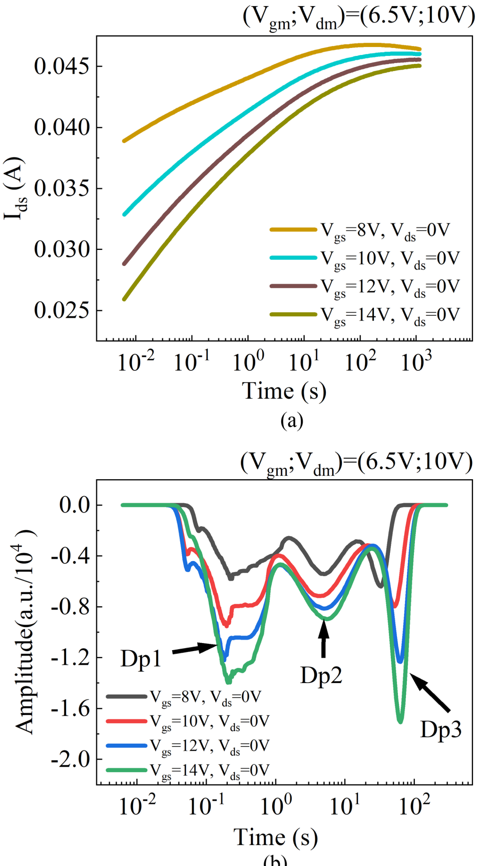

Fig. 8. (a) Transient current curve. (b) TCS when $V_{ds} = 0$ V.

III. Trap Location

To study the trap, we must not only obtain the activation energy of the device but also determine the specific trap location. Due to the different electrical bias conditions (V_{gs} and V_{ds}) during filling, the filling processes of traps at different positions are also different. We therefore applied different electrical biases to the device to fill the traps at different positions in the device, then recorded the transient current curve during the electrons release, and extracted the TCS in each case. Because the area enclosed by each peak in the TCS represents the influence of traps on drain current during recovery. By comparing the variation of TCS of transient drain current during recovery after filling with different electrical biases, a reasonable conclusion can be made on the location of the traps.

A. Traps Filled by Different Gate–Source Voltage

To determine the influence of gate voltage on trap filling, gate–source stress is first applied to the device to fill the traps. To make the time constant peak of traps appear in a more obvious manner, we increased the test voltage V_{dm} to 10 V to produce a more obvious current change. At this level, the power could still be guaranteed to be less than 0.5 W, and the temperature rise could still be ignored. Fig. 8(a) shows the transient current change curve that was obtained when the filling gate voltage changed from 8 to 14 V, and Fig. 8(b) shows the TCS.

As shown in Fig. 8, when the gate voltage increased during filling, three different time constant peaks were obtained, which were designated Dp1, Dp2, and Dp3. The time constant of Dp1 is approximately 100 ms, that of Dp2 is approximately 4 s, and that of Dp3 is approximately 100 s. When the filling gate voltage increased, the peak values of Dp1, Dp2, and Dp3 also increased in tandem. Because these three traps changed significantly with the increases of the filling gate voltage, it can be concluded preliminarily that the three types of trap are all affected by the gate voltage and thus may be located near the gate; however, their specific distribution is worthy of further discussion.

Because the test device is a trench-gate SiC MOSFET, the trap filling caused by the gate voltage will not only occur on both sides of the channel but also will cause trap filling under the gate trench. As a result, the carriers will be injected not only into the SiO_2 layer or the SiC layer on the gate–source side but also into the SiO_2 layer or the SiC layer of the gate–drain structure below the gate trench, as illustrated in Fig. 9. However, it is very obvious that the influence of carriers injected into the gate–source structure on the drain current will be more obvious, because this structure is located in the key position that controls device conduction, and it can thus affect the current directly when the electrons are released. The changes in the amplitudes of the time constant peaks in Fig. 8(b) show that Dp1 and Dp3 vary

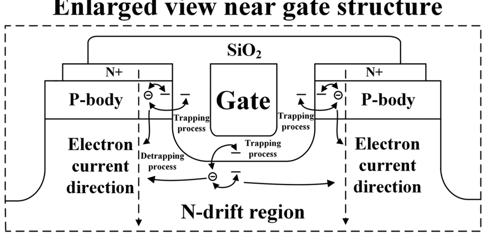

Fig. 9. Schematic diagram of trap filling process.

more obviously with changes in the applied gate voltage, and the changes in their amplitudes are significantly greater than the changes in Dp2. Therefore, it can be inferred from these results that Dp1 and Dp3 may be located at the SiC/SiO_2 interface between the gate and the source at the channel. Additionally, Dp2 may be located at the SiC/SiO_2 interface between the gate and the drain at the bottom of the gate trench. Because it is not located on the main conduction path, its amplitude is relatively less responsive to changes in the gate pressure.

According to the activation energy calculated in Section II-C, Dp2 and Dp3 are the traps in the interface state [32], [33], [34], [35], [36], which have activation energy lower than 0.1 eV of SiC conduction band. And according to [37], there are still other ultrashallow and ultra-deep-level defect distributions after NO nitridation, which further confirms the existence of traps with activation energy below 0.1 eV in the device. Based on the analysis in Section II-C, it can be preliminarily inferred that Dp1 locates in the oxide between the gate and the source, Dp2 is the SiC layer trap between the gate and the drain, and Dp3 is the SiC layer trap between the gate and the source. However, the specific locations of these three traps still require further confirmation.

B. Traps Filled by Different Drain-Source Voltage

To verify the speculation in the preceding section about the trap positions, the influence of the drain bias voltage on the drain current was also measured. On the basis of the preceding experiments, the filling drain voltage was changed from 0 to 10 V, and the other conditions remained unchanged. By performing experiments corresponding to the two groups in the previous section, the specific effects of the drain voltage on the traps in the device were compared. Fig. 10(a) shows the transient current variation curve that was obtained when the filling drain voltage was fixed at 10 V and the filling gate voltage was varied from 8 to 14 V, and Fig. 10(b) shows the calculated TCS.

It is obvious from Fig. 10(a) that after the filling drain voltage was fixed at 10 V, the transient current curves with the filling gate voltages of 8 and 10 V changed obviously, and the curve with the filling gate voltage of 8 V actually changed from its original gradual upward trend to a downward trend. The TCS diagram shows that Dp2 changed significantly; its peak reversed at $V_{gs} = 8$ V, and the peak disappeared completely at $V_{gs} = 10$ V, indicating that the electron capture characteristics of traps had also changed at that stage. With increasing filling gate voltage, Dp2 also played a role in electron release again.

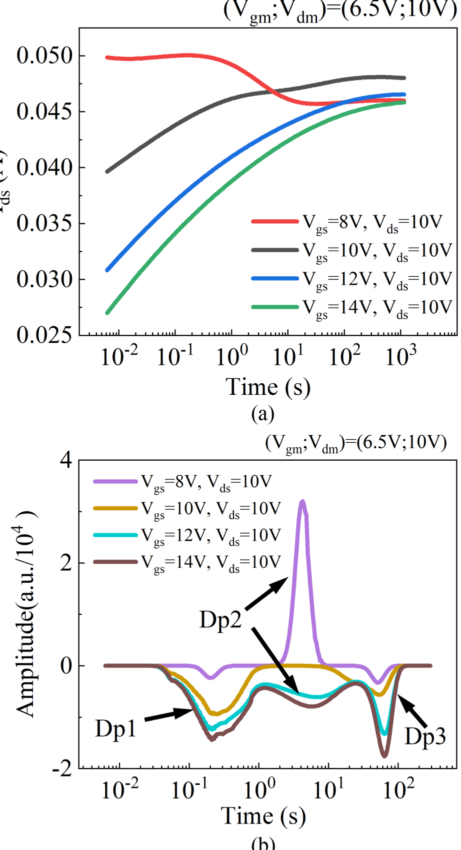

Fig. 10. (a) Transient current curve. (b) TCS when $V_{ds} = 10$ V.

To see the changes in the TCSs more clearly, the TCSs in Fig. 10(b) were compared with that in Fig. 8(b). The comparisons are summarized in Fig. 11 with curves of the same V_{gs} presented in one figure. It can be seen that the time constant in each figure is basically unchanged with the same V_{gs}. In addition, it is worth noting that with the same V_{gs} in each figure, the amplitude of Dp2 is larger under a smaller V_{ds}. It is indicated that an increase in the drain voltage leads to a reduction in the potential difference between the gate and the drain, and a change in the electric field will affect the filling of the traps directly.

For Dp2, when V_{gs} is less than V_{ds} in Fig. 11(a), because an N-drift region exists under the gate trench, the voltage difference between the gate and the drain will be negative, which will then lead to carrier inversion under the gate. The majority carriers that were originally located under the gate trenches change from electrons to holes, as illustrated in Fig. 12(a). The schematic energy band diagram is shown in Fig. 13(a). The holes generated by the negative V_{gd} fill the trap Dp2 at the interface, which finally releases the holes when the trap is released and the total current decreases. And the positive V_{gs} in the SiO_2 layer will also fill Dp1 slightly. So in the TCS, the peak direction of Dp2 is also reversed relative to that at $V_{ds} = 0$ V, and the amplitude of Dp1 is also greatly reduced, as shown in Fig. 11(a). When V_{gs} is equal to V_{ds}, the voltage difference between the gate and the drain is zero. Because the trap filling behavior is caused by the voltage and there is no potential difference between the gate and the drain,

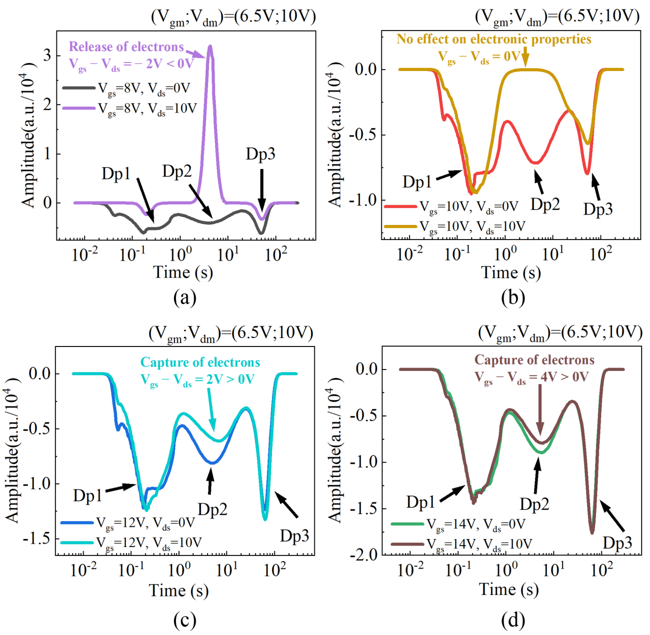

Fig. 11. Comparisons of TCSs with V_{ds} of 10 and 0 V, when V_{gs} is (a) 8 V, (b) 10 V, (c) 12 V, and (d) 14 V.

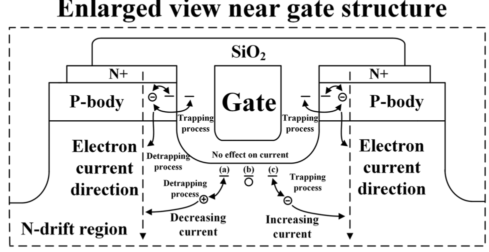

Fig. 12. Schematic diagram of trap release behavior. (a) Trap state under the trench when V_{gs} is less than V_{ds}. (b) Trap state under the trench when V_{gs} is equal to V_{ds}. (c) Trap state under the trench when V_{gs} is greater than V_{ds}.

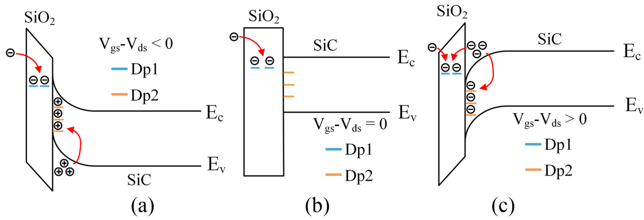

Fig. 13. Energy band diagram below the trench (a) when V_{gs} is less than V_{ds}, (b) when V_{gs} equals to V_{ds}, and (c) when V_{gs} is larger than V_{ds}.

the trap is not then filled, as shown in Fig. 12(b). According to the energy band diagram in Fig. 13(b), since V_{gd} is 0 V, it appears as a nearly flat band and the traps are not filled. The peak in the TCS thus disappears, as shown in Fig. 11(b). When V_{gs} is greater than V_{ds}, the voltage difference between the gate and the drain is positive, the majority carriers accumulate under the gate trench, and the traps capture the electrons, as shown in Fig. 12(c). As illustrated in the energy band diagram in Fig. 13(c), the accumulation of majority carriers happens because the positive V_{gd} fills the trap Dp2, and this causes the current to rise when the electrons are released. At the same time, electrons can also tunnel through the SiO_2 barrier to fill Dp1 slightly. Additionally, as the gate–drain voltage difference increases, the accumulation of the carriers also increases, which results in more electrons being captured by the traps, and the peaks of these traps then gradually increase, as shown in Fig. 11(c) and (d). This further verifies the good response of Dp2 to the gate–drain voltage.

However, because Dp1 and Dp3 are located between the gate and the source, they are affected less strongly by the drain voltage, and thus only show a good response to the gate–source voltage; their peak values in the TCS thus do not change as much as that of Dp2, as shown in Fig. 11(a)–(d). Based on the fact that Dp2 is highly sensitive to changes in the drain voltage, the previous speculation above can be confirmed, and it is thus roughly determined that the position of Dp2 differs significantly from those of Dp1 and Dp3, and it should be the SiC layer trap at the SiC/SiO_2 interface located under the trench.

This trap location distribution can also explain why Dp2 did not show a specific peak in the DLTS testing. When the pulse voltage was applied to the gate and the source of the device during DLTS testing, the transient capacitance change response only reflected the transient capacitance change between the gate and the source. The calculated results only reflect the trap information between the gate and the source. The final results Trp1 and Trp2 corresponded to Dp1 and Dp3, respectively, because their specific locations were between the gate and the source. The possible location of Dp2 is between the gate and the drain, and there is no corresponding peak in the DLTS test results because no pulse voltage is applied between the gate and the drain; additionally, the drift zone between the gate and the drain is very thick, and its capacitance is therefore too small to allow the actual change to be observed.

IV. Conclusion

In this article, three traps designated Dp1, Dp2, and Dp3 in an SiC MOSFET were determined using a transient current method based on Bayesian deconvolution, and their time constants were approximately 0.1, 4, and 100 s, respectively. Through repeated detrapping experiments performed at different temperatures, the activation energies of the Dp2 and Dp3 traps were found to be 0.035 and 0.089 eV, respectively. However, the activation energy of Dp1 could not be calculated. The results were validated by comparison with those from DLTS testing. Both traps with an activation energy of 0.089 eV and trap peaks with an activation energy that could not be calculated were obtained, and the results show good agreement. Finally, by varying the filling voltage conditions, the possible locations of these three traps were preliminarily identified. Dp1 and Dp3 may be located between the gate and the source, where Dp1 is the oxide layer trap, and Dp3 is SiC layer trap the oxide layer trap; Dp2 may also be a SiC layer trap located between the gate and the drain and below the trench. In summary, this article provides a new method for characterization of SiC MOSFET traps, but the

numbers and locations of these traps may vary depending on the device structure. Further research will be required to determine the exact locations of the traps.

In summary, this article provides a new method for characterization of SiC MOSFET traps. The transient current method based on Bayesian deconvolution is used to measure trap information. Compared with other trap characterization methods, the testing instrument and environment of this method are relatively uncomplicated, and the activation energy information as well as TCS of the trap can be obtained simultaneously by measuring the transient drain current change. However, there are also some shortcomings, such as the inability to measure the concentration of traps, and the inability to characterize specific interfacial trap density information. At the same time, because the method relies on time constant information for trap characterization, it cannot distinguish traps with the same time constant. But through the integration of the TCS image, the specific impact of each trap on the current can be recognized and the trap quantity information can also be reflected, which is worth further study.

References

[1] J. Millan, P. Godignon, X. Perpina, A. Perez-Tomas, and J. Rebollo, "A survey of wide bandgap power semiconductor devices," *IEEE Trans. Power Electron.*, vol. 29, no. 5, pp. 2155–2163, May 2014.

[2] J. Weckbrodt, N. Ginot, C. Batard, and S. Azzopardi, "Monitoring of gate leakage current on SiC power MOSFETs: An estimation method for smart gate drivers," *IEEE Trans. Power Electron.*, vol. 36, no. 8, pp. 8752–8760, Aug. 2021.

[3] L. Spaziani and L. Lu, "Silicon, GaN and SiC: There's room for all: An application space overview of device considerations," in *Proc. IEEE 30th Int. Symp. Power Semicond. Devices ICs*, Chicago, IL, USA, 2018, pp. 8–11, doi: 10.1109/ISPSD.2018.8393590.

[4] J. Chen, X. Du, Q. Luo, X. Zhang, P. Sun, and L. Zhou, "A review of switching oscillations of wide bandgap semiconductor devices," *IEEE Trans. Power Electron.*, vol. 35, no. 12, pp. 13182–13199, Dec. 2020.

[5] M. Xie, P. Sun, K. Wang, Q. Luo, and X. Du, "Online gate-oxide degradation monitoring of planar SiC MOSFETs based on gate charge time," *IEEE Trans. Power Electron.*, vol. 37, no. 6, pp. 7333–7343, Jun. 2022.

[6] P. Fiorenza, F. Giannazzo, and F. Roccaforte, "Characterization of SiO_2/4H-SiC interfaces in 4H-SiC MOSFETs: A review," *Energies*, vol. 12, no. 12, 2019, Art. no. 2310, doi: 10.3390/en12122310.

[7] L. C. Yu, G. T. Dunne, K. S. Matocha, K. P. Cheung, J. S. Suehle, and K. Sheng, "Reliability issues of SiC MOSFETs: A technology for high-temperature environments," *IEEE Trans. Device Mater. Rel.*, vol. 10, no. 4, pp. 418–426, Dec. 2010.

[8] T. Nguyen, A. Ahmed, T. V. Thang, and J. Park, "Gate oxide reliability issues of SiC MOSFETs under short-circuit operation," *IEEE Trans. Power Electron.*, vol. 30, no. 5, pp. 2445–2455, May 2015.

[9] S. E. Tyaginov et al., "Physical principles of self-consistent simulation of the generation of interface states and the transport of hot charge carriers in field-effect transistors based on metal-oxide-semiconductor structures," *Phys. Semicond. Devices*, vol. 52, pp. 242–247, 2018, doi: 10.1134/S1063782618020203.

[10] X. She, A. Q. Huang, O. Lucia, and B. Ozpineci, "Review of silicon carbide power devices and their applications," *IEEE Trans. Ind. Electron.*, vol. 64, no. 10, pp. 8193–8205, Oct. 2017.

[11] J. O. Gonzalez and O. Alatise, "Impact of BTI-induced threshold voltage shifts in shoot-through currents from crosstalk in SiC MOSFETs," *IEEE Trans. Power Electron.*, vol. 36, no. 3, pp. 3279–3291, Mar. 2021.

[12] M. Ostling, R. Ghandi, and C. Zetterling, "SiC power devices—Present status, applications and future perspective," in *Proc. IEEE 23rd Int. Symp. Power Semicond. Devices ICs*, 2011, pp. 10–15.

[13] H. A. Moghadam, S. Dimitrijev, J. Han, D. Haasmann, and A. Aminbeidokhti, "Transient-current method for measurement of active near-interface oxide traps in 4H-SiC MOS capacitors and MOSFETs," *IEEE Trans. Electron Devices*, vol. 62, no. 8, pp. 2670–2674, Aug. 2015.

[14] T. Hatakeyama, M. Sometani, K. Fukuda, H. Okumura, and T. Kimoto, "Characterization of traps in SiC/SiO_2 interfaces close to the conduction band by deep-level transient spectroscopy," *Jpn. J. Appl. Phys.*, vol. 54, no. 11, 2015, Art. no. 111301, doi: 10.7567/JJAP.54.111301.

[15] M. Hauck, J. Weisse, J. Lehmeyer, G. Pobegen, H. B. Weber, and M. Krieger, "Quantitative investigation of near interface traps in 4H-SiC MOSFETs via drain current deep level transient spectroscopy," *Mater. Sci. Forum*, vol. 897, pp. 111–114, 2017, doi: 10.4028/www.scientific.net/MSF.897.111.

[16] H. Okada, "Characterization of SiO_2/SiC near-interface oxide traps with constant-capacitance deep-level transient spectroscopy," *Mater. Sci. Forum*, vol. 963, pp. 213–216, 2019, doi: 10.4028/www.scientific.net/MSF.963.213.

[17] K. Yamasue, Y. Yamagishi, and Y. Cho, "Influence of non-uniform interface defect clustering on field-effect mobility in SiC MOSFETs investigated by local deep level transient spectroscopy and device simulation," *Mater. Sci. Forum*, vol. 1004, pp. 627–634, 2020, doi: 10.4028/www.scientific.net/MSF.1004.627.

[18] J. Joh and J. A. Del Alamo, "A current-transient methodology for trap analysis for GaN high electron mobility transistors," *IEEE Trans. Electron Devices*, vol. 58, no. 1, pp. 132–140, Jan. 2011.

[19] D. Bisi et al., "Deep-level characterization in GaN HEMTs-part I: Advantages and limitations of drain current transient measurements," *IEEE Trans. Electron Devices*, vol. 60, no. 10, pp. 3166–3175, Oct. 2013.

[20] S. Pan et al., "Identifying the properties of traps in GaN high-electron-mobility transistors via amplitude analysis based on the voltage-transient method," *IEEE Trans. Electron Devices*, vol. 68, no. 11, pp. 5541–5546, Nov. 2021.

[21] X. Zheng, S. Feng, Y. Gao, Y. Zhang, Y. Jia, and S. Pan, "A voltage-transient method for characterizing traps in GaN HEMTs," *Microelectron. Rel.*, vol. 93, pp. 57–60, 2019, doi: 10.1016/j.microrel.2018.12.009.

[22] M. Tapajna, R. J. T. Simms, Y. Pei, U. K. Mishra, and M. Kuball, "Integrated optical and electrical analysis: Identifying location and properties of traps in AlGaN/GaN HEMTs during electrical stress," *IEEE Electron Device Lett.*, vol. 31, no. 7, pp. 662–664, Jul. 2010.

[23] T. J. Kennett, W. V. Prestwich, and A. Robertson, "Bayesian deconvolution I: Convergent properties," *Nucl. Instrum. Methods*, vol. 151, no. 1/2, pp. 285–292, 1978, doi: 10.1016/0029-554X(78)90502-5.

[24] T. J. Kennett, W. V. Prestwich, and A. Robertson, "Bayesian deconvolution II: Noise properties," *Nucl. Instrum. Methods*, vol. 151, no. 1/2, pp. 293–301, 1978, doi: 10.1016/0029-554X(78)90503-7.

[25] T. J. Kennett, P. M. Brewster, W. V. Prestwich, and A. Robertson, "Bayesian deconvolution III: Applications and algorithm implementation," *Nucl. Instrum. Methods*, vol. 153, no. 1, pp. 125–135, 1978, doi: 10.1016/0029-554X(78)90628-6.

[26] V. Szekely, A. Poppe, and M. Rencz, "Algorithmic extension of thermal field solvers: Time constant analysis," in *Proc. IEEE 16th Annu. Semicond. Thermal Meas. Manage. Symp.*, 2000, pp. 99–107.

[27] T. Aichinger, G. Rescher, and G. Pobegen, "Threshold voltage peculiarities and bias temperature instabilities of SiC MOSFETs," *Microelectron. Rel.*, vol. 80, pp. 68–78, 2018, doi: 10.1016/j.microrel.2017.11.020.

[28] R. E. Kremer, M. C. Arikan, J. C. Abele, and J. S. Blakemore, "Transient photoconductivity measurements in semi-insulating GaAs. I. An analog approach," *J. Appl. Phys.*, vol. 62, no. 6, pp. 2424–2431, 1987, doi: 10.1063/1.339849.

[29] A. K. Agarwal, S. Seshadri, and L. B. Rowland, "Temperature dependence of Fowler-Nordheim current in 6H- and 4H-SiC MOS capacitors," *IEEE Electron Device Lett.*, vol. 18, no. 12, pp. 592–594, Dec. 1997.

[30] P. Fiorenza, A. Frazzetto, A. Guarnera, M. Saggio, and F. Roccaforte, "Fowler-Nordheim tunneling at SiO_2/4H-SiC interfaces in metal-oxide-semiconductor field effect transistors," *Appl. Phys. Lett.*, vol. 105, no. 14, 2014, Art. no. 142108, doi: 10.1063/1.4898009.

[31] P. Fiorenza et al., "Temperature-dependent Fowler-Nordheim electron barrier height in SiO_2/4H-SiC MOS capacitors," *Mater. Sci. Semicond. Process.*, vol. 78, pp. 38–42, 2018, doi: 10.1016/j.mssp.2017.11.024.

[32] A. F. Basile, J. Rozen, J. R. Williams, L. C. Feldman, and P. M. Mooney, "Capacitance-voltage and deep-level-transient spectroscopy characterization of defects near SiO_2/SiC interfaces," *J. Appl. Phys.*, vol. 109, no. 6, 2011, Art. no. 064514, doi: 10.1063/1.3552303.

[33] E. Murakami, T. Furuichi, T. Takeshita, and K. Oda, "Suppression of PBTI of SiC-MOSFETs under 100 kHz gate-switching operation by using a gate off-voltage of -5 V," *Mater. Sci. Forum*, vol. 924, pp. 711–714, 2018, doi: 10.4028/www.scientific.net/MSF.924.711.

[34] G. Y. Chung et al., "Interface state density and channel mobility for 4H-SiC MOSFETs with nitrogen passivation," *Appl. Surf. Sci.*, vol. 184, no. 1, pp. 399–403, 2001, doi: 10.1016/S0169-4332(01)00684-5.

[35] S. Dhar et al., "Nitrogen and hydrogen induced trap passivation at the SiO_2/4H-SiC interface," *Mater. Sci. Forum*, vol. 527–529, pp. 949–954, 2006, doi: 10.4028/www.scientific.net/MSF.527-529.949.

[36] P. Fiorenza, F. Giannazzo, S. Cascino, M. Saggio, and F. Roccaforte, "Identification of two trapping mechanisms responsible of the threshold voltage variation in SiO_2/4H-SiC MOSFETs," *Appl. Phys. Lett.*, vol. 117, no. 10, 2020, Art. no. 103502, doi: 10.1063/5.0012399.

[37] A. F. Basile et al., "Effect of NO annealing on 6H- and 4H-SiC MOS interface states," *Mater. Sci. Forum*, vol. 645–648, pp. 499–502, 2010, doi: 10.4028/www.scientific.net/MSF.645-648.499.

Shan Jiang received the B.S. degree in electronic science and technology, in 2020, from Beijing University of Technology, Beijing, China, where since 2020, he has been working toward the master's degree in electronic science and technology with the Laboratory of Semiconductor Device Reliability Physics.

His research interests include the reliability and trap characterization of silicon carbide devices.

Meng Zhang received the B.S. and M.S. degrees in electronic science and technology from the University of Electronic Science and Technology of China, Chengdu, China, in 2010 and 2013, respectively, and the Ph.D. degree in electronic science and technology from the Department of Industrial and Systems Engineering, Hong Kong Polytechnic University, Hong Kong, in 2018.

After graduation, she was a Postdoctoral Researcher with the College of Physics and Optoelectronic Engineering, Shenzhen University, Shenzhen, China. In 2021, she joined Beijing Technology of University, Beijing, China, where she is currently a Lecturer. Her current research interests include novel power semiconductor devices and reliability.

Xianwei Meng received the B.S. degree in electronic science and technology, in 2020, from Beijing University of Technology, Beijing, China, where since 2020, he has been working toward the master's degree in electronic science and technology with the Laboratory of Semiconductor Device Reliability Physics.

His research interests include the reliability and thermal measurement of silicon carbide and gallium nitride devices.

Xiang Zheng received the Ph.D. degree in electronic science and technology from Beijing University of Technology, Beijing, China, in 2020.

He is currently a Postdoctoral Researcher with the School of Physics, University of Bristol, Bristol, U.K. His research interests include thermal management and electrical performance characterization of wide bandgap semiconductors.

Shiwei Feng received the B.S. and M.S. degrees in electronic science and technology from Jilin University, Changchun, China, in 1983 and 1986, respectively, and the Ph.D. degree in electronic science and technology from Beijing University of Technology, Beijing, China, in 1999.

He was a Postdoctoral Researcher with Howard University, Washington, DC, USA, in 2000, and with Rutgers University, Newark, NJ, USA, from 2001 to 2002. In 1986, he joined Beijing University of Technology where he is currently a Professor with the Faculty of Information Technology. His current research interests include reliability physics of semiconductor devices and thermal management of semiconductor devices.

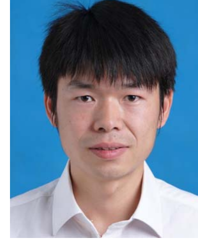

Yamin Zhang received the Ph.D. degree in microelectronics and solid-state electronics from the Laboratory of Semiconductor Device Reliability Physics, Beijing University of Technology, Beijing, China, in 2015.

In 2015, he joined Beijing University of Technology where he is currently an Associate Professor. His research interests include the noninvasive thermal measurement and thermal management of semiconductor devices.